



# Efficient hydrogen production from methane over iridium-doped ceria catalysts synthesized by solution combustion

Georgeta Postole\*, Thanh-Son Nguyen, Mimoun Aouine, Patrick Gélin, Luis Cardenas, Laurent Piccolo\*

Institut de Recherches sur la Catalyse et l'Environnement de Lyon (IRCELYON), CNRS & Université Lyon 1, 2 Avenue Albert Einstein, 69626 Villeurbanne Cedex 9, France



## ARTICLE INFO

### Article history:

Received 30 June 2014

Received in revised form 14 October 2014

Accepted 13 November 2014

Available online 22 November 2014

### Keywords:

Iridium

Ceria

Solution combustion synthesis

Heterogeneous catalysis

Steam reforming of methane

## ABSTRACT

This study reports on the investigations performed on an Ir-CeO<sub>2</sub> (0.1 wt% Ir) catalyst, prepared for the first time by one-step solution combustion synthesis (SCS) and submitted to a number of analyses: N<sub>2</sub> volumetry, elemental analysis, X-ray diffraction, scanning electron microscopy, aberration-corrected high-resolution transmission electron microscopy, X-ray photoelectron spectroscopy, and temperature-programmed methods. The catalyst was studied in the steam reforming of methane (SRM) at 750 °C, under water-deficient conditions (CH<sub>4</sub>/H<sub>2</sub>O ratio of 10) and in the presence of 220 ppm H<sub>2</sub>S. The obtained catalytic performances were compared with those of an Ir/CeO<sub>2</sub> catalyst prepared by incipient wetness impregnation (IWI). The influence of the support and the metal was investigated through testing of Ir/SiO<sub>2</sub>-Al<sub>2</sub>O<sub>3</sub>-IWI and Rh-CeO<sub>2</sub>-SCS catalysts, respectively. Using CeO<sub>2</sub> as carrier, Ir-based catalysts are highly efficient in SRM and resistant to carbon and irreversible sulfur poisoning. The catalytic activity of Ir-CeO<sub>2</sub>-SCS is superior to that of Ir/CeO<sub>2</sub>-IWI. Unlike the Ir-CeO<sub>2</sub> catalyst, Ir/SiO<sub>2</sub>-Al<sub>2</sub>O<sub>3</sub> is completely deactivated in presence of sulfur, while Rh-CeO<sub>2</sub>-SCS does not recover its initial activity after exposure to an H<sub>2</sub>S-containing feed.

© 2014 Elsevier B.V. All rights reserved.

## 1. Introduction

The main advantage of solid oxide fuel cells (SOFCs), operating at high temperatures (600–1000 °C) and using ceramic membranes that conduct oxygen anions, is their capacity to operate not only with hydrogen but also with hydrocarbon-based fuels, such as natural gas [1]. The operation of SOFCs fed with natural gas is based on the internal conversion of methane, on the anode side, to produce H<sub>2</sub> and CO by reforming reactions (“direct internal reforming”). Nickel–yttria-stabilized zirconia (Ni-YSZ) is the most commonly used material for fabricating SOFC anodes and works satisfactorily with H<sub>2</sub> because of the high electrocatalytic activity of Ni [2,3]. Unfortunately, with natural gas under cell operation conditions the dissociative adsorption of CH<sub>4</sub> on the anode surface competes with the desired reforming processes, resulting in uncontrolled carbon deposition [4]. Furthermore, S-containing compounds found as impurities in hydrocarbon-based fuels react with the nickel surface

to form very stable Ni<sub>x</sub>S<sub>y</sub> compounds, which block reactant access to the Ni surface [5].

In order to mitigate the issue of carbon formation over Ni-YSZ anodes, the deposition of a catalytically active layer onto the anodic electrode was first applied for operation in CO<sub>2</sub>/isooctane mixtures [6]. Strong improvements with respect to operation without the catalytic barrier could be achieved, but carbon formation on the catalyst could not be totally avoided. The concept was extended to the use of chemically inert barrier layers added to commercial Ni-YSZ anodes for operation with methane [7]. This architecture was successful to extend the range of coke-free operation, even with pure methane. The main role of the inert barrier layer is to impede the transport of electrochemically formed products from the three-phase region toward the fuel channel, thus inhibiting coking and facilitating the reforming process. It helps also preventing the direct contact of the Ni anode with high hydrocarbon concentrations. Further, a concept of gradual internal reforming (GIR) was proposed for SOFCs fed with hydrocarbon fuels (e.g. methane) [8,9]. The principle is that SRM and electrochemical oxidation of hydrogen can be self-sustained, because the latter reaction produces the water needed by the former one. The main advantages of GIR are a delocalization of the high endothermicity

\* Corresponding authors. Tel.: +33 427465734.

E-mail addresses: [georgeta.postole@ircelyon.univ-lyon1.fr](mailto:georgeta.postole@ircelyon.univ-lyon1.fr) (G. Postole), [laurent.piccolo@ircelyon.univ-lyon1.fr](mailto:laurent.piccolo@ircelyon.univ-lyon1.fr) (L. Piccolo).

of steam reforming and a potential operation in dry methane after initiation of the reforming reaction with a small amount of steam [8,9]. The practical applicability of such an SOFC architecture was demonstrated for a system continuously operated with hydrogen, methane, and ethanol, without water, O<sub>2</sub>, or CO<sub>2</sub> additions, delivering a rather stable power output for nearly 400 h [10].

Noble metals (NMs) such as Pt-group ones, which are too expensive to be used in conventional industrial reformers, can be materials of choice for the barrier layer in the anode compartment of SOFCs integrating a GIR concept and directly fed with natural gas. NM-based catalysts present high activity in methane reforming, durability, low coking tendency, and resistance to poisoning by sulfur. Thus, they may be used for the production of synthesis gas at very low steam/carbon ratios [11–13]. As the use of GIR requires the development of specific catalysts moderately active in steam reforming but highly resistant to carbon deposition, the efficiency of NM-based catalysts with low metal loading (much lower than 30–40 wt% typically used for Ni-based steam reforming catalysts) can minimize the cost, making them versatile for this application. The literature concerning steam reforming of hydrocarbons on NM-based catalysts shows the use of 0.1 up to 5 wt% NM loadings. Furthermore, as seen in Table 1 which summarizes literature findings [11,13–24] for SRM over NM catalysts, most of these studies were performed under oxidative atmosphere (H<sub>2</sub>O/C ratio higher than unity), between 350 and 750 °C. Even though a rigorous comparison of the data is difficult due to the variety of experimental conditions (temperature, pressure, reactant gas composition) and catalyst characteristics (metal dispersion, support type), these reports demonstrated that SRM proceeds with high activity and stability over metals such as Ru, Rh, Ir, Pd, Pt. Wei and Iglesia [17,21,23,24] have found that, whatever the nature of the NM, the SRM reaction rate increases linearly with CH<sub>4</sub> pressure, but it is not influenced neither by H<sub>2</sub>O nor by the nature of the support. These observations are in line with those reported by Berman et al. [25] who carried out the reaction at high temperatures (700–900 °C) over a Ru-based catalyst. Conversely, at low temperatures (450–500 °C), the reaction order toward methane was found much less than unity. Gorte et al. [15,26] have found that ceria-supported NMs are much more active than NMs supported on inert oxides. Mortola et al. [22] have demonstrated that, when Pt is supported on a material containing CeO<sub>2</sub>, its dispersion does not have a crucial influence on the number of converted CH<sub>4</sub> molecules. The stability and activity of the SRM catalysts depend on the balance between the rate of methane decomposition over the metal particles and the rate of carbon removal. Due to its redox properties, ceria promotes the oxidation of carbonaceous adsorbates [27].

This work is an extension of the studies dealing with the development of NM-based catalysts for hydrogen production from CH<sub>4</sub>/H<sub>2</sub>O mixtures, for both SOFC and automotive applications (CH<sub>4</sub> can be eliminated from automotive exhaust streams by SRM in reducing environments, and the produced H<sub>2</sub> can serve as a NO reductant [26]). Based on the preliminary experience acquired in the use of iridium-based catalysts for SOFC applications [9,28,29], this study has been focused on a non-conventional one-step method for the preparation of Ir-doped ceria, namely solution combustion synthesis (SCS). It is well known that the method of preparation and the applied treatment affect the strength of metal-support interaction and the metal dispersion, which in turn strongly influence the final performances of dispersed metal catalysts. SCS has been recently used to prepare catalysts for reforming and combustion reactions, and even to synthesize advanced materials for SOFCs [30,31]. To the best of our knowledge, the present work is the first attempt to synthesize Ir-based catalysts by such a method. It involves the one-pot combustion of cerium and metal

salts in the presence of water and a fuel, and generates high degree of metal dispersion [32,33].

In this paper, after a brief report on structural aspects (this part will be detailed elsewhere [34]), it will be shown how the catalyst can be best activated for SRM and how it compares to other types of catalysts (preparation method, support, metal) in terms of activity, stability and resistance to irreversible sulfur poisoning. In addition, the role of Ir doping and of S reacted with the catalyst are revealed by temperature-programmed reduction with methane and X-ray photoelectron spectroscopy.

## 2. Experimental

### 2.1. Materials synthesis

For the preparation of pure CeO<sub>2</sub>, the solution contained (NH<sub>4</sub>)<sub>2</sub>Ce(NO<sub>3</sub>)<sub>6</sub> [Sigma Aldrich, 99.99%] and NH<sub>2</sub>CH<sub>2</sub>COOH [Sigma Aldrich, 99%] (glycine, used as the fuel) in the molar ratio 1:2.67. These values were chosen to obtain stoichiometric proportions of oxidizer and fuel, i.e., with the oxidizing/reducing valence ratio of the redox mixture equal to 1 [35]. For the preparation of 0.1 wt% Ir–CeO<sub>2</sub>, 10<sup>−3</sup> mol% of (NH<sub>4</sub>)<sub>2</sub>IrCl<sub>6</sub> [Strem Chemicals, 99%] was additionally employed. Practically, a 300 cm<sup>3</sup> borosilicate beaker containing a mixture of (NH<sub>4</sub>)<sub>2</sub>Ce(NO<sub>3</sub>)<sub>6</sub> (5.00 g) and glycine (1.82 g) without/with (NH<sub>4</sub>)<sub>2</sub>IrCl<sub>6</sub> (4 mg for 0.1 wt% Ir–CeO<sub>2</sub>), and 30 mL of deionized water, was introduced into a muffle furnace (Carbolite ELF 11/6) maintained at 350 °C. At the point of complete dehydration (within 5–10 min), the solution started to boil with frothing and foaming, and ignition took place after a few seconds with rapid increase of the temperature (up to ca. 1000 °C) simultaneously to the evolution of a large quantity of gases. This yielded a voluminous solid product within a few minutes. In order to verify the reproducibility of the SCS preparation, three different batches of Ir–CeO<sub>2</sub> catalysts were similarly synthesized and named: Ir–CeO<sub>2</sub>, Ir–CeO<sub>2</sub>(2) and Ir–CeO<sub>2</sub>(3).

On the basis of thermogravimetric measurements (see Section 3), CeO<sub>2</sub> could be used as-prepared for the catalytic investigations, while for Ir–CeO<sub>2</sub> a thermal treatment was required. In this work, four different thermal treatments were applied to the Ir–CeO<sub>2</sub> reference sample, as described in Table 2. In all cases, the temperature was increased with a heating rate of 5 °C min<sup>−1</sup> up to the desired value, and a total flow rate of 7 L<sub>NTP</sub> h<sup>−1</sup> was used, irrespective of the atmosphere chosen for the pretreatment.

For comparison, a Rh–CeO<sub>2</sub> catalyst was prepared by SCS using the same procedure and RhCl<sub>3</sub> [Aldrich, 38–40% in water] as the NM precursor. The as-prepared powder containing 0.05 wt% Rh (number of metal atoms similar as in the 0.1 wt% Ir) was submitted to an oxido-reducing treatment, as described for the Ir–CeO<sub>2</sub>-oxred catalyst. The obtained catalyst is denoted Rh–CeO<sub>2</sub>-oxred.

In addition, an Ir/CeO<sub>2</sub> catalyst was prepared by conventional IWI of ceria, itself prepared by SCS. For the impregnation step, Ir(C<sub>5</sub>H<sub>7</sub>O<sub>2</sub>)<sub>3</sub> (acetylacetonate, Sigma-Aldrich, purity 97%) was dissolved in toluene using the concentration needed to obtain the desired Ir loading (0.1 wt%, measured loading 0.14 wt%). The sample was allowed to mature in ambient conditions for 2 h and dried at 120 °C overnight, then treated under pure hydrogen flow at 500 °C for 6 h. This led to well-dispersed iridium particles with sizes in the same range as found for the SCS catalysts, i.e. 1–3 nm (Table 3). The obtained powder is denoted Ir/CeO<sub>2</sub>-IWI.

Finally, a so-called Ir/ASA catalyst was prepared by IWI of amorphous silica–alumina (Sasol SICAL-40, 500 m<sup>2</sup> g<sup>−1</sup>, pre-calcined in air at 550 °C for 3 h), using the same impregnation-reduction procedure. The catalyst loading was 0.22 wt% and the Ir particle size was 1.4 ± 0.3 nm.

**Table 1**  
Overview of the literature data for CH<sub>4</sub> steam reforming reaction over NM-based catalysts.

Catalyst	NM loading (wt%)	T (K)	Total pressure/total flow rate	Reactant mixture ratio	TOF (s <sup>-1</sup> )	r <sub>CH<sub>4</sub></sub> (mol g <sub>cat</sub> <sup>-1</sup> s <sup>-1</sup> )	E <sub>a</sub> (kJ mol <sup>-1</sup> )	Ref.
Pd/Al <sub>2</sub> O <sub>3</sub>	1.0	783	1 atm 291 mL min <sup>-1</sup>	CH <sub>4</sub> /H <sub>2</sub> O = 1/3 (n.s.)	0.9	2.9 × 10 <sup>-19</sup>	96	[14]
Pd/CeO <sub>2</sub>	1.0	783	1 atm 291 mL min <sup>-1</sup>	CH <sub>4</sub> /H <sub>2</sub> O = 1/3 (n.d.)	4.1	3.9 × 10 <sup>-19</sup>	71	[14]
Pd/CeO <sub>2</sub>	1.0	620–770	1 atm 120 mL min <sup>-1</sup>	CH <sub>4</sub> /H <sub>2</sub> O = 1/2 (6.6% CH <sub>4</sub> )	n.s.	n.s.	57	[15]
Ru/ZrO <sub>2</sub> –La <sub>2</sub> O <sub>3</sub>	4.0	823	1 atm 100 mL min <sup>-1</sup>	CH <sub>4</sub> /H <sub>2</sub> O = 1/1 (8.0% CH <sub>4</sub> )	n.s.	10.2 × 10 <sup>-5</sup>	n.d.	[16]
Ru/γ-Al <sub>2</sub> O <sub>3</sub>	1.6	873	≈1–5 atm 100 mL min <sup>-1</sup>	CH <sub>4</sub> /H <sub>2</sub> O = 1/1 (20.0% CH <sub>4</sub> )	4.9	n.s.	n.d.	[17]
Ru/γ-Al <sub>2</sub> O <sub>3</sub>	3.2	873	≈1–5 atm 100 mL min <sup>-1</sup>	CH <sub>4</sub> /H <sub>2</sub> O = 1/1 (20.0% CH <sub>4</sub> )	3.3	n.s.	n.d.	[17]
Ru/ZrO <sub>2</sub>	3.2	873	≈1–5 atm 100 mL min <sup>-1</sup>	CH <sub>4</sub> /H <sub>2</sub> O = 1/1 (20.0% CH <sub>4</sub> )	2.3	n.s.	n.d.	[17]
Ru/ZrO <sub>2</sub>	1.0	773	≈1.3 atm 202 mL min <sup>-1</sup>	CH <sub>4</sub> /H <sub>2</sub> O = 1/4 (16.7% CH <sub>4</sub> )	11.1	n.s.	n.d.	[13]
BaRh <sub>x</sub> Zr <sub>1-x</sub> O <sub>3</sub>	5.0	723–1023	1 atm n.s.	CH <sub>4</sub> /H <sub>2</sub> O = 1/3 (n.s.)	n.s.	n.s.	69	[18]
Rh/Ce <sub>0.6</sub> Zr <sub>0.4</sub> O <sub>2</sub>	0.8	823	≈1.5 atm n.s.	CH <sub>4</sub> /H <sub>2</sub> O/H <sub>2</sub> = 1/4/0.7 (n.s.)	n.s.	1.0 × 10 <sup>-5</sup>	n.d.	[19]
Rh/CeO <sub>2</sub>	0.1	773	≈1.2 atm 200 mL min <sup>-1</sup>	CH <sub>4</sub> /H <sub>2</sub> O = 1/3 (5.0% CH <sub>4</sub> )	n.s.	3.6 × 10 <sup>-5</sup>	n.d.	[20]
Rh/ZrO <sub>2</sub>	0.1	773	≈1.2 atm 200 mL min <sup>-1</sup>	CH <sub>4</sub> /H <sub>2</sub> O = 1/3 (5.0% CH <sub>4</sub> )	n.s.	3.9 × 10 <sup>-5</sup>	n.d.	[20]
Rh/Al <sub>2</sub> O <sub>3</sub>	0.4	873	≈1 atm n.s.	CH <sub>4</sub> /H <sub>2</sub> O = 1/1.25 (20.0% CH <sub>4</sub> )	4.1	n.s.	109	[21]
Rh/ZrO <sub>2</sub> <sup>a</sup>	1.0	773	1 atm 360 mL min <sup>-1</sup>	CH <sub>4</sub> /H <sub>2</sub> O/H <sub>2</sub> = 1/4/0.4 (19.0% CH <sub>4</sub> )	12.5	n.s.	n.d.	[11]
Pt/Ce <sub>0.5</sub> La <sub>0.5</sub> Al	1.0	773	1 atm 100 mL min <sup>-1</sup>	CH <sub>4</sub> /H <sub>2</sub> O/H <sub>2</sub> = 1/3/0.5 (n.s.)	3.5	5.2 × 10 <sup>-5</sup>	66	[22]
Pt/ZrO <sub>2</sub> <sup>a</sup>	1.0	773	1 atm 360 mL min <sup>-1</sup>	CH <sub>4</sub> /H <sub>2</sub> O/H <sub>2</sub> = 1/4/0.4 (19.0% CH <sub>4</sub> )	2.5	n.s.	n.d.	[11]
Pt/ZrO <sub>2</sub>	1.6	873	1 atm n.s.	CH <sub>4</sub> /H <sub>2</sub> O = 1/1.25 (20.0% CH <sub>4</sub> )	13.1	n.s.	75	[23]
Ir/ZrO <sub>2</sub> <sup>a</sup>	1.0	773	1 atm 360 mL min <sup>-1</sup>	CH <sub>4</sub> /H <sub>2</sub> O/H <sub>2</sub> = 1/4/0.4 (19.0% CH <sub>4</sub> )	2.3	n.s.	n.d.	[11]
Ir/ZrO <sub>2</sub>	0.8	873	1 atm n.s.	CH <sub>4</sub> /H <sub>2</sub> O = 1/1.25 (20.0% CH <sub>4</sub> )	12.4	n.s.	87	[24]

<sup>a</sup> 3 at% Y-stabilized ZrO<sub>2</sub> support. The results obtained in [11] for the catalysts investigated after varying aging treatments are not given here. n.s. = not specified; n.d. = not determined.

## 2.2. Materials characterization

The concentrations of iridium were determined by inductively coupled plasma-optical emission spectroscopy (ICP-OES, Activa instrument from Horiba Jobin Yvon). In order to dissolve them completely, the samples were treated with a mixture of H<sub>2</sub>SO<sub>4</sub>, aqua regia and HF at 250–300 °C. The residual chloride was dosed by combustion/ionic chromatography coupling.

Elemental sulfur analysis in reacted samples was performed with a ThermoFisher Flash 2000 CHNS analyzer. Portions of samples with a mass of 1 mg were weighed in tin containers. The samples were burnt in a vertical reactor (oxidation tube) in the dynamic

mode at 950 °C in a He flow (140 mL min<sup>-1</sup>) by adding 90 mL of O<sub>2</sub> at the time of sample introduction.

Specific surface area measurements were performed by N<sub>2</sub> adsorption volumetry at –196 °C using the BET method (ASAP 2010M instrument from Micromeritics). Prior to surface area determination, the powders were outgassed at 300 °C for 2 h in secondary vacuum.

Powder X-ray diffraction (XRD) patterns were collected at room temperature (RT) under air, using a Bruker D8A25 diffractometer (Cu Kα radiation at 0.154184 nm) equipped with a Ni filter and a 1-D fast multistrip detector (LynxEye, 192 channels on 2.95°). Diffractograms were collected at 2θ between 20° and 80° with steps of

**Table 2**  
Conditions used during the thermal treatments applied to the as-prepared Ir-CeO<sub>2</sub> catalyst.

Atmosphere during treatment	Temperature (°C) Duration (h)	Temperature (°C) Duration (h)	Temperature (°C) Duration (h)	Temperature (°C) Duration (h)
12% O <sub>2</sub> in N <sub>2</sub>	–	500 2	–	300 2
N <sub>2</sub>	500 2	–	–	300–500 1 at 300 °C
12% H <sub>2</sub> in N <sub>2</sub>	–	–	500 2	500 2
Sample abbreviation	Ir-CeO <sub>2</sub> -inert	Ir-CeO <sub>2</sub> -ox	Ir-CeO <sub>2</sub> -red	Ir-CeO <sub>2</sub> -oxred <sup>*</sup>

<sup>\*</sup> The freshly prepared sample was heated to 300 °C (5 °C min<sup>-1</sup>) in a flow of 12% O<sub>2</sub> in N<sub>2</sub> and maintained at this temperature for 2 h. At this temperature, the atmosphere was switched from O<sub>2</sub>/N<sub>2</sub> to N<sub>2</sub> and maintained for 1 h. The temperature was then increased to 500 °C (5 °C min<sup>-1</sup>) and switched from N<sub>2</sub> to 12% H<sub>2</sub> in N<sub>2</sub>, with a plateau of 2 h at this temperature.

**Table 3**  
Physico-chemical properties of CeO<sub>2</sub> and Ir-CeO<sub>2</sub> catalysts.

Sample	SA <sup>a</sup> (m <sup>2</sup> g <sup>-1</sup> )	Ir <sup>b</sup> (wt%)	CS <sup>c</sup> (nm)	a <sup>c</sup> (Å)	d <sub>Ir</sub> <sup>d</sup> (nm)	D <sup>e</sup> (%)
CeO <sub>2</sub>						
Fresh	22	–	50	5.4123(1)	–	–
Tested	~6	–	85	5.4122(1)	–	–
Ir-CeO <sub>2</sub> -oxred						
Fresh	~15	0.11	37	5.4125(1)	1.7 ± 0.9	59
Tested	~7	n.d.	60	5.4120(1)	1.8 ± 0.5	56
Ir/CeO <sub>2</sub> -IWI						
Fresh	16	0.14	31	5.4161(1)	1.3 ± 0.5	77
Tested	~8	n.d.	n.d.	n.d.	1.6 ± 0.8	63

<sup>a</sup> Specific surface area (SA) determined by BET analysis. The values marked with ~ were determined indirectly from correlations with XRD sizes.

<sup>b</sup> Concentrations of Ir determined by ICP-OES.

<sup>c</sup> Average crystallite size (CS) and lattice parameter (a) of ceria, as derived from Rietveld analysis of XRD data.

<sup>d</sup> Average Ir particle diameter and standard deviation determined from TEM.

<sup>e</sup> The metal dispersion was estimated from the mean particle size using  $D = 1/d_{Ir}$ .

0.02° and a time per step of 4 s (total acquisition time of 237 min). Phase identification was performed using the Diffrac.Eva software (Bruker) and the ICDD-PDF4+ database. The lattice parameters and the crystallite sizes were determined by the Rietveld method (Fullprof code; the full program and documentation can be obtained at <http://www.ill.eu/sites/fullprof>).

Thermogravimetric measurements combined with differential thermal analysis and mass spectrometry (TG-DTA-MS) were performed with a Setsys Evolution-1200 instrument from Setaram, coupled with a mass spectrometer (Omnistar from Pfeiffer) through a capillary system. The experiments were performed by heating 15 mg of the sample located in a 100 µL Pt crucible from RT up to 900 °C with a heating rate of 5 °C min<sup>-1</sup> under argon flow (50 mL min<sup>-1</sup>). The MS was set at specific *m/z* values in order to follow the possible formation of H<sub>2</sub>, H<sub>2</sub>O, N<sub>2</sub>, NH<sub>3</sub>, NO<sub>x</sub>, O<sub>2</sub>, CO, CO<sub>2</sub>, C<sub>2</sub>H<sub>4</sub>, CH<sub>2</sub>N, C<sub>2</sub>H<sub>5</sub>NO<sub>2</sub>, CNCH<sub>3</sub>, Cl<sub>2</sub>, HCl, and CH<sub>3</sub> Cl.

The sample morphology and atomic structure were examined by scanning electron microscopy (SEM) and aberration-corrected high-resolution transmission electron microscopy (HRTEM), respectively. The SEM images were obtained with a Jeol JSM 5800LV microscope, whereas the HRTEM pictures were recorded using an FEI Titan G2 aberration-corrected ETEM operating at 300 kV with 1 Å best resolution. From the HRTEM images, the metal nanoparticle diameters were determined using their projected areas, assuming that they are spherical.

X-ray photoelectron spectroscopy (XPS) was performed in order to get insight into the chemical changes that occur on the catalyst surface during testing in the presence of H<sub>2</sub>S. To this aim, the reactor containing the spent sample was purged with N<sub>2</sub> at the reaction temperature for 5 min after testing, quenched to RT in N<sub>2</sub> (Linde, N5.0 purity), closed, and then transferred to a glove box where the sample could be removed from the reactor and placed in a hollowed-out stainless steel sample holder. The sample was then transferred under Ar atmosphere, via a portable transfer cell, from the glove box into the XPS chamber, thereby avoiding exposure to ambient air. The fresh samples were also analyzed for comparison.

The XPS analyses were carried out using a commercial instrument (Axis Ultra DLD spectrometer from Kratos Analytical), with monochromatized Al Kα source (1486.6 eV). The analysis revealed well-resolved peaks corresponding to O 1s, Ir 4f, S 2p and Ce 3d. Each high-resolution spectrum was decomposed into a combination of Voigt functions, and Ce 3d was fitted using a linear combination of the experimental spectra of Ce<sup>3+</sup> and Ce<sup>4+</sup> [36]. All peaks were calibrated using the C 1s component of adventitious carbon as the spectral reference, which was fixed at 284.6 eV.

### 2.3. Catalytic activity and temperature-programmed measurements

Catalytic activity experiments were carried out in a continuous flow system at atmospheric pressure and 750 °C, using a tubular U-shaped quartz reactor (internal diameters of 15 and 4 mm for CeO<sub>2</sub> and NM-based catalysts, respectively). Prior to the catalytic tests, the samples (100 mg for CeO<sub>2</sub> and 10 mg for NM-based catalysts) were treated in N<sub>2</sub> flow (7 L<sub>NTP</sub> h<sup>-1</sup>) at 900 °C for 2 h. The reactant mixture consisted of 50 vol% CH<sub>4</sub> and 5 vol% H<sub>2</sub>O in N<sub>2</sub> at a total flow rate of 7 L<sub>NTP</sub> h<sup>-1</sup>. Suitable water vapor concentration in the reaction mixture was obtained by flowing the adequate mixture of CH<sub>4</sub> and N<sub>2</sub> dry gases throughout a saturator containing distilled water, and maintained at 33.1 °C. The inlet and outlet gas lines of the reactor were kept at 67 °C by heating tapes in order to avoid condensation. An M&C ECP gas cooler maintained at 3 °C was used to reduce the steam concentration in the feed in order to allow for a reliable analysis by gas chromatography. CH<sub>4</sub>, H<sub>2</sub>, CO, and CO<sub>2</sub> were analyzed with a Varian micro-GC equipped with molecular sieve 5 Å and Porapak Q columns, and a thermal conductivity detector (TCD). CH<sub>4</sub> (N5.5 purity) and N<sub>2</sub> (N5.0 purity) were supplied by Linde. The catalyst resistance to sulfur poisoning was evaluated at 750 °C by adding H<sub>2</sub>S (220 ppm) to the reaction mixture. The mixture of 506 ppm H<sub>2</sub>S and N<sub>2</sub> was supplied by Linde (N5.0 purity for N<sub>2</sub> in the mixture). The reactor effluents were sampled every 5 min and simultaneously analyzed on line by the µGC. After exposure to sulfur, regeneration experiments were also conducted by returning directly to a reforming S-free gas mixture.

The carbon mass balance, defined as the fraction of all the carbon atoms recovered at the reactor outlet (CO, CH<sub>4</sub>, and CO<sub>2</sub>) over all carbon atoms fed into the reactor (CH<sub>4</sub>), was observed within 95% for all experiments. Differential conditions were used for all measurements, the maximum CH<sub>4</sub> conversions being less than 7% (the reaction rate is independent of the H<sub>2</sub>O partial pressure [24,37]). All measurements were carried out far from SRM equilibrium with  $\eta_{SRM} < 1.3 \times 10^{-4}$ . The equilibrium approach,  $\eta_{SRM}$ , is defined from the SRM thermodynamic reaction data ( $K_{eq,SRM} = 47.2 \text{ atm}^2$  at 750 °C) and the measured partial pressures  $P_i$  of reactants and products as:

$$\eta_{SRM} = \frac{P_{CO} P_{H_2}^3}{P_{CH_4} P_{H_2O}} \cdot \frac{1}{K_{eq,SRM}}$$

The CH<sub>4</sub> conversion ( $X_{CH_4}$ ), CH<sub>4</sub> consumption rate and H<sub>2</sub>, CO, and CO<sub>2</sub> formation rates were calculated as described elsewhere [38].

Temperature-programmed reduction (CH<sub>4</sub>-TPR) was performed under diluted dry methane (3 mol% CH<sub>4</sub> in N<sub>2</sub>) before and after the reforming reaction, for a better understanding of the catalytic steps involving CH<sub>4</sub>. The bench used for these experiments was the same as for catalytic testing. Before performing CH<sub>4</sub>-TPR, the fresh



samples were pretreated under nitrogen flow ( $7 \text{ L}_{\text{NTP}} \text{ h}^{-1}$ ) at  $900^\circ\text{C}$  for 2 h. For TPR on the tested catalysts, immediately after the SRM reaction the reactor was purged with nitrogen and cooled down to RT. The samples were then heated at  $5^\circ\text{C min}^{-1}$  to  $900^\circ\text{C}$  in the gas mixture.

The possible formation of carbon deposits on the tested catalysts was checked by temperature-programmed oxidation (TPO) to evaluate the nature, reactivity and amount of coke, if any. As for  $\text{CH}_4$ -TPR, immediately after the SRM tests, the reactor was purged with nitrogen and cooled down to RT in the same atmosphere. Then, a mixture of 3 mol%  $\text{O}_2$  in  $\text{N}_2$  (flow rate of  $7 \text{ L}_{\text{NTP}} \text{ h}^{-1}$ ) was introduced and the temperature was linearly increased with a heating rate of  $5^\circ\text{C min}^{-1}$  from room temperature to  $900^\circ\text{C}$ . The  $\text{O}_2$  consumption and the possible formation of CO and  $\text{CO}_2$  were quantified by gas chromatography and were used to calculate the amount of deposited carbon.

### 3. Results and discussion

#### 3.1. Structural characteristics of the catalysts prepared by SCS

The SCS-prepared 0.1 wt% Ir-CeO<sub>2</sub> samples, namely Ir-CeO<sub>2</sub>, Ir-CeO<sub>2</sub>(2) and Ir-CeO<sub>2</sub>(3), after similar oxido-reductive pretreatments, yielded reproducible catalytic performances in SRM, as reported later on. Thus, this study reports mainly the investigations performed on the reference Ir-CeO<sub>2</sub> catalyst, which was submitted to a number of structural analyses and catalytic tests.

After synthesis, thermogravimetric measurements (TG-DTA-MS) were performed in order to follow the evolution of both Ir-CeO<sub>2</sub> and CeO<sub>2</sub> during a thermal treatment under an inert atmosphere, similar to that applied before catalytic testing. The results are presented in Fig. S1. For CeO<sub>2</sub>, it can be seen that a mass loss of less than 1% is observed from RT to  $900^\circ\text{C}$ , due to water removal below  $400^\circ\text{C}$ . This indicates that the combustion reaction was complete, leading to a solid product free of organic residues. Conversely, Ir-CeO<sub>2</sub> loses almost 18% of its initial mass, mostly below  $300^\circ\text{C}$ . In the TG profile of the Ir-CeO<sub>2</sub> powder, the weight loss below  $140^\circ\text{C}$  is due to water removal. The important weight decrease from  $150$  to  $300^\circ\text{C}$  is attributed to the exothermic desorption and decomposition of residual glycine and precursors, with production of  $\text{NH}_3$ ,  $\text{H}_2\text{O}$ ,  $\text{CO}_2$ , and NO. The weight loss continues up to  $750^\circ\text{C}$ . In Fig. S1c, the evolution of the product distribution shows that the retention of a significant fraction of residual organic species took place during the Ir-CeO<sub>2</sub> preparation process. This indicates incomplete combustion of fuel or/and oxidant. It must be pointed out that, for both CeO<sub>2</sub> and Ir-CeO<sub>2</sub> preparations, the ratio of fuel and oxidant was fixed in such a way that the net reducing valency of the fuel equaled the net oxidizing valency of the oxidant. The origin of the discrepancy between CeO<sub>2</sub> and Ir-CeO<sub>2</sub> behaviors might be the interaction between the Ir precursor and the glycine, with the formation of a stable complex such as  $[\text{Ir}(\text{gly})_3\text{Cl}]^-$  [39], which would lead to charring of the fuel.

Based on these results, CeO<sub>2</sub> was further used as-prepared, while an additional thermo-chemical treatment was necessary for the Ir-based sample after the combustion process to burn away the residual organic species retained in the ceria matrix or adsorbed at its surface. The effect of a series of oxidation and/or reduction treatments on the Ir-CeO<sub>2</sub> catalytic performances will be addressed in the following section. Based on catalytic results, the most effective treatment was found to be an oxidation at  $300^\circ\text{C}$  followed by a reduction at  $500^\circ\text{C}$ . The physico-chemical characterization data relative to the as-prepared CeO<sub>2</sub> sample and the Ir-CeO<sub>2</sub> powder, both fresh and treated by oxido-reduction (Ir-CeO<sub>2</sub>-oxred), are reported in Table 3. The amount of Ir present in the final catalyst (0.11 wt%) is close to the target loading (0.10 wt%), and the chlorine

amount is below the detection level (5 wt ppm). The XPS analyses confirmed the absence of chlorine on the catalyst surface.

The XRD patterns (Fig. S2) for as-prepared (fresh) CeO<sub>2</sub> and Ir-CeO<sub>2</sub>-oxred samples correspond to the cubic fluorite-like structure of CeO<sub>2</sub> (ICDD code: 04-008-6546). The BET surface areas of as-prepared and spent (SRM-tested) ceria are 22 and  $6 \text{ m}^2 \text{ g}^{-1}$ , respectively (Table 3).

For Ir-CeO<sub>2</sub>, no diffraction peaks due to iridium were observed, owing to the facts that the Ir content in the catalyst is low, and the Ir species are highly dispersed on the support. The addition of iridium at dopant level did not induce changes in the lattice parameter of ceria but favored the formation of slightly smaller ceria crystallites (CS), as shown in Table 3. Similarly, a reduction in the average pore diameter of CeO<sub>2</sub> was observed by Gayen et al. [40] when preparing Rh-CeO<sub>2</sub> catalysts by SCS. Gonzalez-Delacruz et al. [41] studied Ni/CeO<sub>2</sub> catalysts prepared by combustion synthesis for dry reforming of methane, and found that with increasing amounts of Ni (from 7 to 26 wt%), the CeO<sub>2</sub> crystallite size decreases (from 22 to 10 nm, respectively). The decrease in the average crystallite size in Ir-CeO<sub>2</sub>, as compared to pure CeO<sub>2</sub>, is likely due to metallic ions diffusing to the surface during synthesis, hindering the growth of CeO<sub>2</sub> crystallites, as also suggested by Bera et al. [42] for Cu-CeO<sub>2</sub> prepared by SCS. The Rietveld analysis of the diffractograms for the Ir-CeO<sub>2</sub> powder did not reveal any structural change induced by the thermal treatment. The values of  $5.4124(1) \text{ \AA}$  for the lattice parameter and 38 nm for the average crystallite size in the case of fresh Ir-CeO<sub>2</sub> are similar to those obtained after oxred treatment. XRD measurements also demonstrated that the SRM-tested ceria-based powders retain the fluorite structure, but the crystallite sizes increase due to heating up to  $900^\circ\text{C}$  (during catalytic testing, no further increase in the grain sizes was observed), consistently with the decrease of the surface area (Table 3).

CeO<sub>2</sub> and Ir-CeO<sub>2</sub>-oxred were observed by SEM in order to obtain information concerning the pore structure, an important parameter for successful use of such materials in SOFC anodes. As shown by Fig. 1a, the CeO<sub>2</sub> powder displays a sponge-like structure with a lot of cracks and pores associated with the rapid evolution of gases during the combustion process. Fig. 1b shows that a network of interconnected pores is also present in the microstructure of the Ir-CeO<sub>2</sub>-oxred catalyst. Fig. 1c and d presents aberration-corrected HRTEM images of SCS-prepared Ir-CeO<sub>2</sub> before (Fig. 1c) and after (Fig. 1d) catalytic testing in SRM at  $750^\circ\text{C}$ . At high resolution, ceria grains exhibit a layered structure [34], explaining the presence of Moiré patterns in Fig. 1c. Another feature characteristic of SCS-prepared ceria-based catalysts is the presence of round holes in the ceria structure, as the one visible in Fig. 1c. In addition, Ir particles dispersed in the size range 1–3 nm on the surface of CeO<sub>2</sub> grains (main image, Fig. 1c) or at grain boundaries (inset). The high-resolution image in inset shows an Ir particle exposing (111) and (100) facets. These images were recorded for a sample treated by oxidation–reduction (Table 2). On the as-prepared Ir-CeO<sub>2</sub> sample, IrO<sub>x</sub> nanoparticles were detected, although iridium could also be present as cations substituted to Ce ones in the ceria matrix, as reported by Hegde et al. [32] on the basis of XRD results for Pt-, Pd- and Rh-CeO<sub>2</sub> catalysts synthesized by SCS. In the present study, XRD data neither support nor rule out this statement, due to the low amount of metal used (0.1 wt%).

After exposure to the severe conditions employed in SRM, ceria exhibits a similar atomic-scale morphology as immediately after the oxidation–reduction treatment, and faceted Ir nanoparticles with essentially unchanged size (Table 3) are still visible. Fig. 1d shows an example of Ir nanoparticle in epitaxy on a (100) facet of a ceria crystallite. Fig. 1e and f shows TEM images of the Ir/CeO<sub>2</sub> catalyst prepared by impregnation, before and after testing in SRM, respectively. The fresh sample shows the presence of a large number of Ir particles of 1–3 nm in diameter, with a mean particle

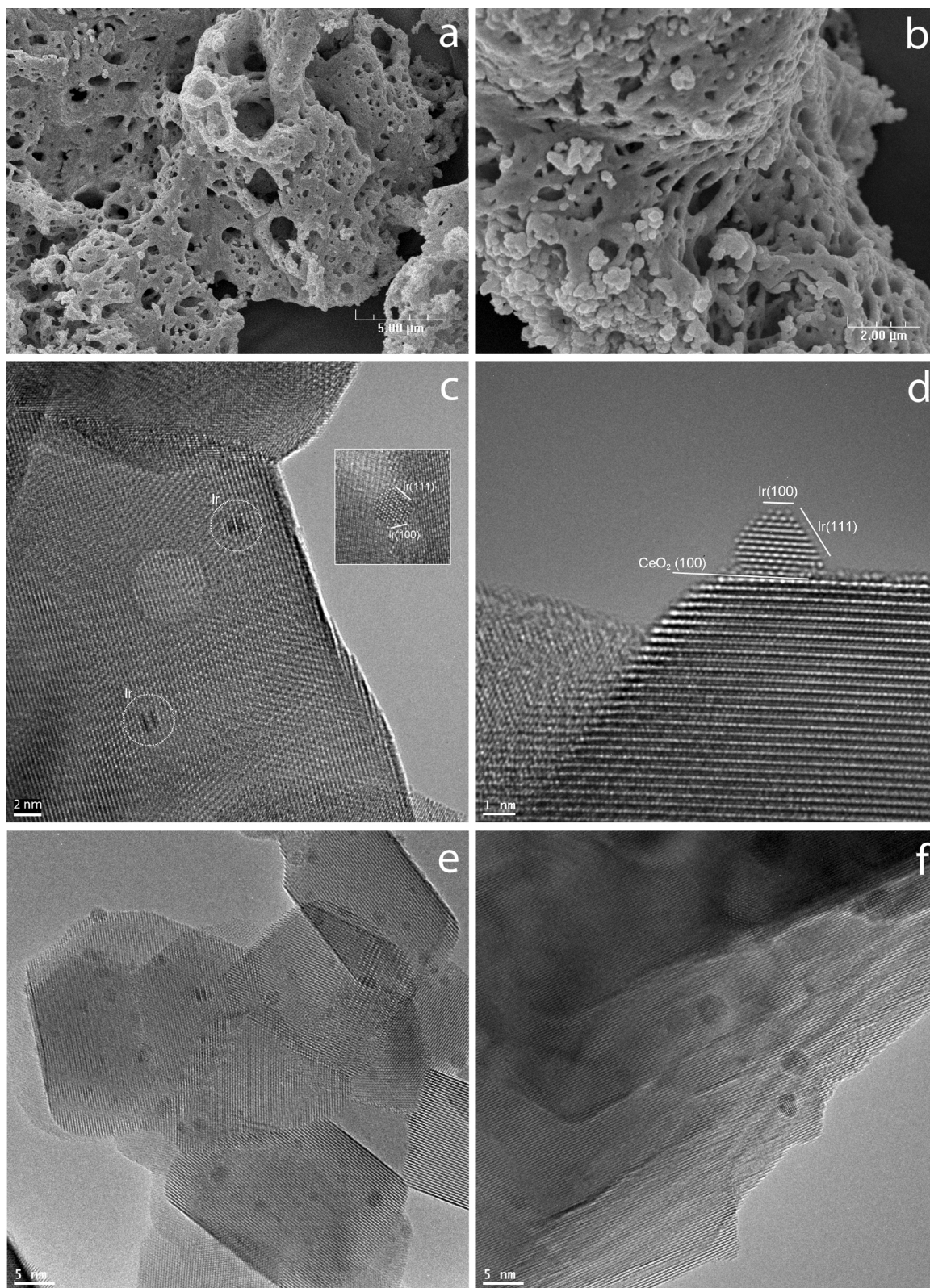


**Fig. 1.** (a) and (b) SEM image of a fracture surface of fresh  $\text{CeO}_2$  (a) and Ir- $\text{CeO}_2$ -oxred (b). (c)–(f) Aberration-corrected HRTEM images of Ir- $\text{CeO}_2$ -oxred (c) and (d) and Ir/ $\text{CeO}_2$ -red (e) and (f). (c) and (e) images were obtained before, while (d) and (f) micrographs were recorded after catalytic test. Ir nanoparticles are indicated by circles in (c). Inset: atomic-scale resolution image of an Ir nanoparticle (same scale as main image).

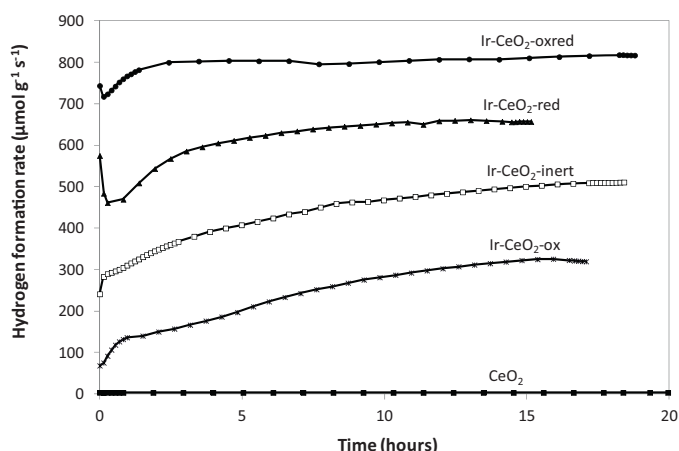


**Fig. 2.** H<sub>2</sub> formation rate as a function of time during SRM over CeO<sub>2</sub> and Ir-CeO<sub>2</sub> catalysts at 750 °C. Before catalytic testing, all the samples (100 mg CeO<sub>2</sub> and 10 mg Ir-CeO<sub>2</sub>) were pretreated under N<sub>2</sub> at 900 °C for 2 h. The catalytic tests were performed in the presence of a reactant mixture containing 50 vol% CH<sub>4</sub> and 5 vol% H<sub>2</sub>O in N<sub>2</sub> (7 L<sub>NTP</sub> h<sup>-1</sup>).

size of 1.3 nm. After 15 h testing in SRM, the mean particle size is somewhat greater (1.6 nm), and the Ir particles appear scarcer and mostly located at ceria grain boundaries.

### 3.2. Effect of the catalyst pretreatment on the SRM activity – reproducibility

The simplicity, fastness and low cost of SCS make it an attractive approach for producing technologically useful materials [30]. Many essential parameters regarding combustion synthesis have been extensively discussed in literature, like the type and amount of organic fuel, the role of pH, the effect of various combustion aids and inert salts, the difference between wet and dry combustions, the ignition mode and temperature, etc. However, the influence of thermochemical treatments on the structural and catalytic properties of SCS catalysts have been rarely addressed (and the catalysts have been often used either “as-prepared” or precalcined at high temperature), even though they can have crucial impact on the final catalyst properties [22,43]. Furthermore, no information about the reproducibility of the SCS preparation method is given in the literature for NM-based materials. Both aspects are addressed here.

Since the Ir-CeO<sub>2</sub> catalyst was prepared by combustion synthesis for the first time, it was necessary to optimize the post-treatment with regard to the targeted reaction. Thus, the effect of inert (“inert”), oxidizing (“ox”), reducing (“red”), or oxidizing then reducing (“oxred”) treatments on the Ir-CeO<sub>2</sub> performances in SRM was investigated. Before the catalytic testing and irrespective of the treatment applied after synthesis, the catalysts were activated under N<sub>2</sub> at 900 °C for 2 h.

The performances of Ir-CeO<sub>2</sub> after the thermal treatments are presented in comparison with the performances of pure CeO<sub>2</sub> in Fig. 2, Table 4, and Table S1.

CeO<sub>2</sub> presents a measurable catalytic activity (Fig. S3) for methane conversion at 750 °C under the highly water-deficient conditions (H<sub>2</sub>O/CH<sub>4</sub> = 0.1) used, H<sub>2</sub> and CO<sub>2</sub> being the main products with small amounts of CO. As compared to that of CeO<sub>2</sub>, the activity of Ir-CeO<sub>2</sub>-inert is greatly increased, with a rate of hydrogen formation of two orders of magnitude higher (Table 4). Moreover, the methane consumption rate increases continuously with time-on-stream, as can be seen in Table S1. Interestingly, calcination is detrimental to the catalytic activity of Ir-CeO<sub>2</sub> with respect to the inert treatment. However, as seen in Fig. 2, the activity of Ir-CeO<sub>2</sub>-ox

is still significantly higher than that of CeO<sub>2</sub> and the catalyst continuously activates during testing. In spite of their different activities, it is likely that a continuous structural reorganization of the Ir-CeO<sub>2</sub>-inert and Ir-CeO<sub>2</sub>-ox catalysts takes place under the reaction mixture, giving rise to new sites with enhanced catalytic activity.

The steam reforming process is performed under strongly reducing conditions. Thus, in order to verify if the continuous increase of activity during catalytic testing can be related to an in situ catalyst reduction, a treatment under hydrogen was imposed to the fresh Ir-CeO<sub>2</sub> sample. It is observed that the reducing treatment has a remarkable promoting effect on the activity of Ir-CeO<sub>2</sub>. The methane conversion rate of Ir-CeO<sub>2</sub>-red follows a similar behavior as the one observed for the Ir-CeO<sub>2</sub>-inert and -ox catalysts. However, the steady state is achieved faster, within ca. 10 h (see Fig. 2 and Table S1).

Given that the surface residues originating from the catalyst preparation may play a role in the catalyst performances, the evolved gases during the reducing and oxidizing treatments were quantified. Following the temperature-programmed experiments reported in Fig. S4, it appears that not all carbonaceous species were burnt away in the presence of hydrogen at up to 500 °C (1.6 and 1.1 mmol<sub>CO<sub>x</sub></sub> g<sub>cat</sub><sup>-1</sup> were evolved during the ox and red treatments, respectively). No direct correlation could be established between the presence of carbonaceous species and the treatment-dependent activities. However, in accordance with the TG-DTA-MS data obtained under inert atmosphere, these results suggest that a calcination step is needed to remove any organic content, followed by a reduction to favor the formation of active Ir sites. As seen in Table 4 and Fig. 2, the activity of Ir-CeO<sub>2</sub>-red is surpassed when the fresh catalyst is submitted to the oxido-reducing treatment. Ir-CeO<sub>2</sub>-oxred achieved steady steam reforming within 2 h and its activity remained constant for another 15 h on stream. The formation of metallic iridium nanoparticles after the oxido-reducing treatment was confirmed by HRTEM (Fig. 1c). Using the metal dispersion obtained for the tested powder after 15 h of reaction (Table 3), a TOF value of 8 s<sup>-1</sup> was found for Ir-CeO<sub>2</sub>-oxred.

As shown by Table 4, the addition of Ir to CeO<sub>2</sub> not only strongly increases the low activity of ceria, but affects the product distribution. In all cases, the products obtained at quasi-steady state after 15 h on stream, were H<sub>2</sub>, CO, and CO<sub>2</sub> with a CO<sub>2</sub>/CO molar ratio varying from 3 for CeO<sub>2</sub> to 0.16 for Ir-CeO<sub>2</sub>-oxred. The measured concentrations of reactants and products during SRM (Table S2) show that the water-gas shift reaction (WGS: CO + H<sub>2</sub>O → CO<sub>2</sub> + H<sub>2</sub>) is equilibrated during CH<sub>4</sub> reforming (CH<sub>4</sub> + H<sub>2</sub>O → CO + 3H<sub>2</sub>) on Ir-CeO<sub>2</sub>-inert, -red and -oxred at 750 °C ( $\eta_{\text{WGS}}$  = 0.89–1.07, Table 4). An apparent activation energy of 30 kJ mol<sup>-1</sup> is found for Ir-CeO<sub>2</sub>-oxred (Fig. S5), which is consistent with the value of 29 kJ mol<sup>-1</sup> reported for dissociative chemisorption of CH<sub>4</sub> on Ir(110) in molecular beam studies [44], and 30 kJ mol<sup>-1</sup> estimated for activation of CH<sub>4</sub> on Ir(111) with density functional theory [45]. This suggests that the C–H bond activation step is rate-determining in the conditions used here. The much higher activation energy value of 157 kJ mol<sup>-1</sup> obtained for Ir-CeO<sub>2</sub>-inert indicates that the nature of the active sites has changed upon oxred treatment.

It can be concluded that the applied treatment is a key parameter for optimizing the performances of the Ir-CeO<sub>2</sub> catalyst in the CH<sub>4</sub>/H<sub>2</sub>O reaction, while keeping a low amount of Ir. Due to the one-pot SCS preparation process, the Ir nanoparticles are strongly anchored to the ceria support and thermally stable over long reaction times, as confirmed by post-reaction TEM (Fig. 1d).

Besides a high activity for methane conversion, the catalyst layer in the SOFC anode compartment should also display a high resistance toward carbon deposition, which may block the active sites for CH<sub>4</sub> reforming and cause cell deterioration. Temperature-programmed oxidation experiments reveal low carbon content on the post-reaction samples (ca. 0.005 and 0.04 wt% C for CeO<sub>2</sub> and



**Table 4**

Comparison of the catalyst performances in SRM.

Sample	Conversion $X_{\text{CH}_4}$ (%)	Rate of $\text{CH}_4$ consumption ( $\mu\text{mol g}^{-1} \text{s}^{-1}$ )	Formation rates ( $\mu\text{mol g}^{-1} \text{s}^{-1}$ )			$\eta_{\text{WGS}}$
			$\text{H}_2$	CO	$\text{CO}_2$	
$\text{CeO}_2$	0.16	0.73 (6.27)	2.9	0.24	0.55	0.15
Ir-CeO <sub>2</sub> -inert	3.93	151	500	105	46.6	0.90
Ir-CeO <sub>2</sub> -ox	2.07	95.7	325	58.0	37.7	0.49
Ir-CeO <sub>2</sub> -red	4.43	201	656	148	52.9	0.89
Ir-CeO <sub>2</sub> -oxred	6.63	258 (16.7)	810	223	35.5	1.07
Ir-CeO <sub>2</sub> (2)-oxred	5.80	228	728	198	33.6	n.d.
Ir-CeO <sub>2</sub> (3)-oxred	5.50	206	688	177	39.3	n.d.
Ir/CeO <sub>2</sub> -IWI-red	4.54	178 (13.2)	577	130	46.6	n.d.
Rh-CeO <sub>2</sub> -oxred	1.61	64.0 (14.4)	220	36.0	28.0	n.d.

Experimental conditions: 750 °C; 5 vol%  $\text{H}_2\text{O}$ , 50 vol%  $\text{CH}_4$ ,  $\text{N}_2$  balance; total flow rate  $7 \text{ L}_{\text{NTP}} \text{ h}^{-1}$ ; 10 mg NM-CeO<sub>2</sub>, 100 mg CeO<sub>2</sub>. Before testing, the samples were heated under  $\text{N}_2$  at 900 °C for 2 h.  $\eta_{\text{WGS}} = (\text{P}_{\text{CO}_2} \text{P}_{\text{H}_2}) / (\text{P}_{\text{CO}} \text{P}_{\text{H}_2\text{O}} K_{\text{eq,WGS}})$ , with  $K_{\text{eq,WGS}} = 1.31$  at 750 °C. Catalyst performances obtained at quasi-steady state, after 15 h of  $\text{CH}_4/\text{H}_2\text{O}$  reaction, in the absence of  $\text{H}_2\text{S}$ . The values of the  $\text{CH}_4$  consumption rates given between brackets were obtained after 2 h of reaction in the presence of 220 ppm  $\text{H}_2\text{S}$ .

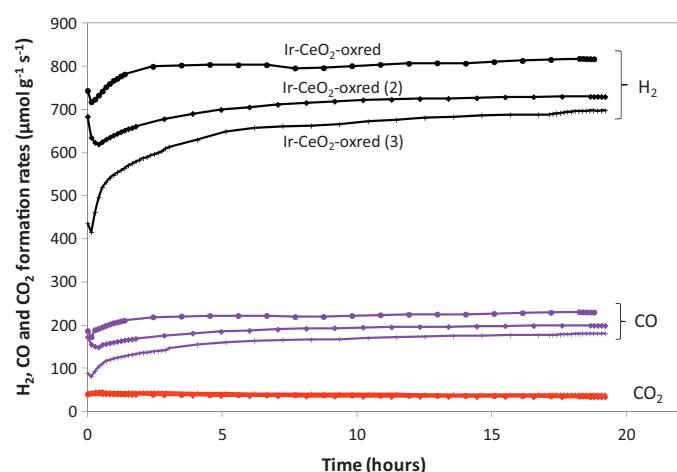


**Fig. 3.**  $\text{H}_2$ , CO, and  $\text{CO}_2$  formation rates as a function of time during SRM over three 0.1 wt% Ir-CeO<sub>2</sub> catalysts (including the one presented in Fig. 2) prepared in the same way, and tested in the same conditions of for Fig. 2.

Ir-CeO<sub>2</sub>-oxred, respectively). As illustrated by Fig. S6, a single  $\text{CO}_2$  peak is observed around 220 °C on the TPO profiles. Although iridium seems to facilitate carbon formation, these results indicate that the carbon issuing from methane decomposition is readily eliminated, which enables a high catalyst stability. In terms of catalyst resistance to the accumulation of carbonaceous species, the use of ceria as carrier is expected to play a key role as oxygen supplier.

In order to assess the reproducibility of the catalyst performances when the SCS route is used as preparation method, two additional 0.1 wt% Ir-CeO<sub>2</sub> catalysts were synthesized and tested in the same conditions as for Fig. 2. The rates of  $\text{H}_2$ , CO and  $\text{CO}_2$  production are shown in Fig. 3 and Table 4. The three Ir-CeO<sub>2</sub>-oxred powders present similar activities. The measured  $\text{CH}_4$  conversion rates are consistent within 15%, which is more than satisfactory taking into account the extremely exothermic conditions applied in SCS [46].

### 3.3. Sulfur-resistance: influence of metal, support, and preparation method

For the target application, it is important to find the catalyst phase providing the best combination of activity, resistance to sulfur poisoning and ease of recovery. Although desulfurization units can be used to significantly reduce the sulfur content in the feed, their inclusion increases the complexity, size and cost of the fuel processing system. Therefore it is desirable to develop catalysts that

are not irreversibly poisoned by the amounts of sulfur commonly found in hydrocarbon-based fuels.

In this work, the sulfur-sensitivity of the catalysts was assessed at 750 °C by adding 220 ppm of  $\text{H}_2\text{S}$  to the  $\text{CH}_4/\text{H}_2\text{O}$  feed. The results in terms of  $\text{H}_2$ , CO, and  $\text{CO}_2$  formation rates are given in Fig. 4a and b for  $\text{CeO}_2$  and Ir-CeO<sub>2</sub>-oxred, respectively. Before  $\text{H}_2\text{S}$  addition, the samples were exposed to a sulfur-free reactant mixture for 18 h at 750 °C in order to reach stable catalytic activity. As mentioned above, in  $\text{H}_2\text{S}$ -free reformat, pure  $\text{CeO}_2$  presents a low activity for  $\text{H}_2$  production. Upon  $\text{H}_2\text{S}$  addition,  $\text{H}_2$ , CO, and  $\text{CO}_2$  are produced in much larger amounts (the rate of methane consumption increases from 0.7 to 6.3%, Table 4), and the enhanced activity remains stable over more than 15 h on stream. Upon suppression of the sulfur source (Fig. 4a), the initial activity is restored. This behavior is consistent with previous findings over doped ceria, showing the promoting influence of  $\text{H}_2\text{S}$  on the  $\text{CH}_4/\text{H}_2\text{O}$  reaction [29,38,47]. Moreover, the selectivity of the reaction to CO with respect to  $\text{CO}_2$  (the CO/ $\text{CO}_2$  molar ratio increases from 0.44 to 1.3 in the presence of  $\text{H}_2\text{S}$ ) increases when adding  $\text{H}_2\text{S}$  to the  $\text{CH}_4/\text{H}_2\text{O}$  mixture.

In order to get insight into the  $\text{H}_2\text{S}$ -induced promotion of ceria activity, an analysis of on-stream  $\text{H}_2\text{S}$  concentration data was carried out (the procedure is described elsewhere [38]). When contacting  $\text{CH}_4/\text{H}_2\text{O}/\text{H}_2\text{S}$  with pure ceria, after an initial consumption of  $\text{H}_2\text{S}$  (up to about 140 ppm), its concentration increases and stabilizes to a constant value of 215 ppm (lower than the 220 ppm added), which indicates some constant and slight  $\text{H}_2\text{S}$  consumption. Indeed, after 2 and 17 h on stream, 0.15 and 0.65 wt% S are consumed, respectively. Interestingly, irrespective of the reaction time in the presence of  $\text{H}_2\text{S}$ , only 0.1 wt% S is found to be adsorbed on ceria, as detected by post-reaction CHNS analysis. This amount corresponds to the  $\text{H}_2\text{S}$  consumed until maximum activity is reached, suggesting that the S-CeO<sub>2</sub> interaction, in the first stage of the reaction, leads to structural changes having positive effects on the catalytic performances. However, no Ce-O-S phase (e.g.  $\text{Ce}(\text{SO}_4)_2$ ,  $\text{Ce}_2(\text{SO}_4)_3$  or  $\text{Ce}_2\text{O}_2\text{S}$ ) is detected by post-reaction XRD, as can be seen in Fig. S2. This implies that the formed phase with enhanced activity is amorphous and/or present only in the near-surface region.

In contrast to ceria, the activity of Ir-CeO<sub>2</sub>-oxred is severely inhibited by exposure to  $\text{H}_2\text{S}$  (Fig. 4b), with a decrease of  $\text{H}_2$  formation rate to ca. 7% of its initial value. However, after the extremely rapid decrease in response to  $\text{H}_2\text{S}$  introduction, the low conversion remains stable for hours on stream. As in the case of pure ceria,  $\text{H}_2\text{S}$  is consumed (1.9 mg S/g<sub>cat</sub> vs 1.5 mg S/g<sub>CeO<sub>2</sub></sub> after 2 h of reaction) when contacted with the Ir-CeO<sub>2</sub>-oxred catalyst, which corresponds to sulfur adsorption on both the carrier and the metal. Upon replacement of the sulfur-containing stream by the original sulfur-free reactant mixture, Ir-CeO<sub>2</sub>-oxred rapidly and almost fully recovers its original activity (Fig. 4b, Table S3). Moreover, this



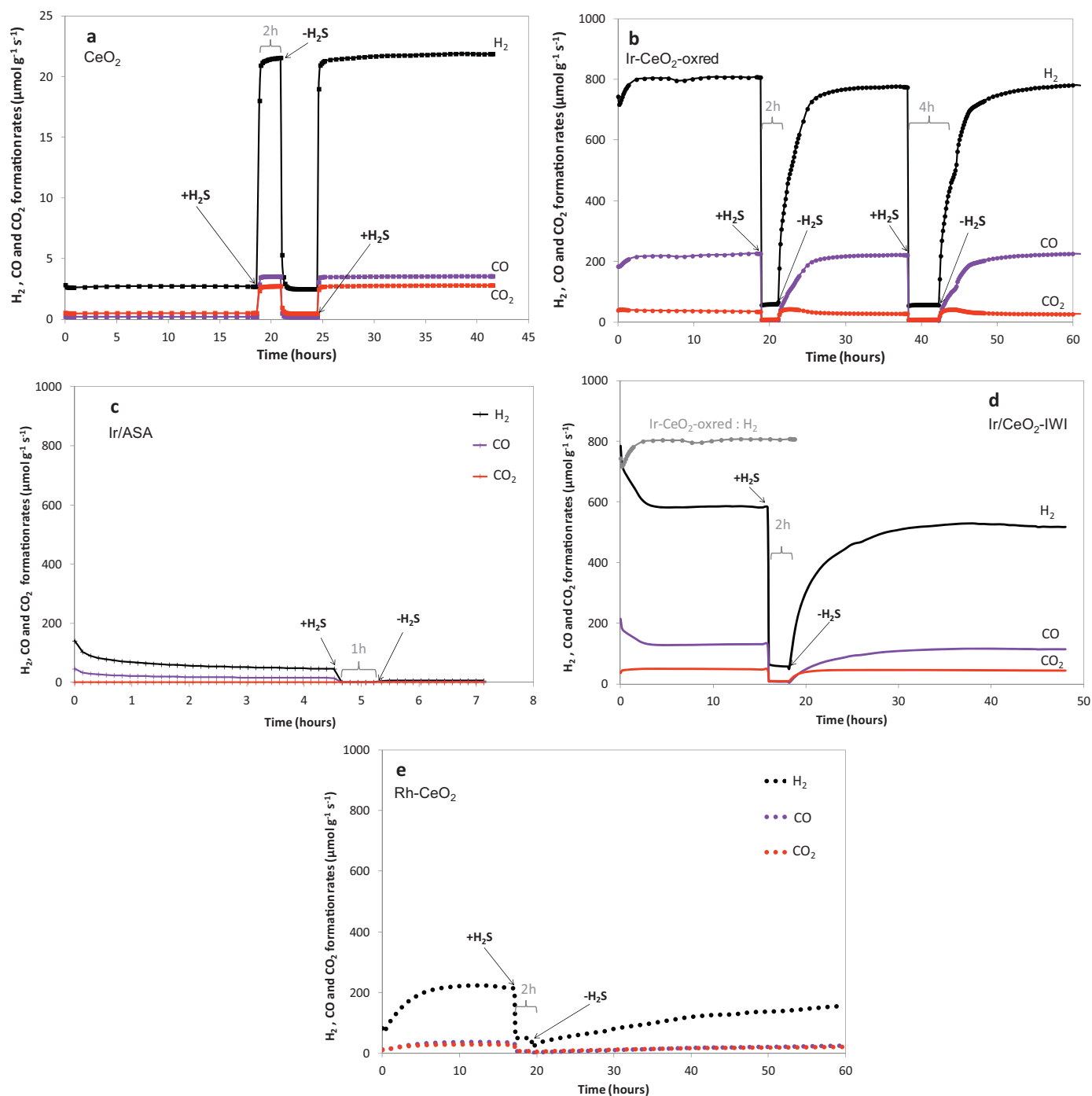


**Fig. 4.**  $\text{H}_2$ , CO, and  $\text{CO}_2$  formation rates as a function of time during SRM at 750 °C over  $\text{CeO}_2$  (a), Ir- $\text{CeO}_2$ -oxred (b), Ir/ASA (c), Ir/ $\text{CeO}_2$ -IWI (d), and Rh- $\text{CeO}_2$  (e). Same conditions as for Fig. 2.  $\text{H}_2\text{S}$  concentration: 220 ppm.

behavior is perfectly reproducible when the reaction is performed again in  $\text{H}_2\text{S}$  presence for a longer time (Fig. 4b). The most probable cause of catalyst deactivation is the metal poisoning by sulfur with the formation of Ir–S chemisorbed species [48]. However, since, in the presence of  $\text{H}_2\text{S}$ , the residual activity of Ir- $\text{CeO}_2$ -oxred (rate of hydrogen formation  $59 \mu\text{mol g}^{-1} \text{s}^{-1}$ ) remains three times higher than that of pure ceria ( $21 \mu\text{mol g}^{-1} \text{s}^{-1}$ ), it can be assumed that the Ir active sites are not completely covered by sulfur. Partly covered Ir metal was already observed under hydrotreating conditions (i.e., in the presence of hydrogen and  $\text{H}_2\text{S}$ ), together with  $\text{Ir}_2\text{S}_3$  and IrS compounds [49].

With the aim of clarifying the role played by ceria in the fast activity recovery observed for Ir- $\text{CeO}_2$ -oxred when the sulfur source is removed from the system, two additional iridium-based catalysts prepared by an IWI method were tested in the same experimental conditions. Firstly, 0.2 wt% iridium supported on amorphous silica–alumina (ASA) was chosen, since it was known to exhibit stable activity in the presence of up to 200 ppm  $\text{H}_2\text{S}$  in tetralin hydroconversion [50]. Its performances in SRM are shown in Fig. 4c. The initial activity of Ir/ASA in SRM is much lower than that of Ir- $\text{CeO}_2$ -oxred, and it continuously decreases on stream in spite of the higher iridium content and much larger surface area

(ca.  $500 \text{ m}^2 \text{ g}^{-1}$  vs. ca.  $15 \text{ m}^2 \text{ g}^{-1}$  for Ir-CeO<sub>2</sub> before testing). When H<sub>2</sub>S is added to the reactant mixture, the Ir/ASA catalyst loses almost completely its activity, which is not anymore recovered after sulfur removal.

Although much more active, Ir/CeO<sub>2</sub>-IWI behaves as Ir/ASA under a clean CH<sub>4</sub>/H<sub>2</sub>O mixture, as presented in Fig. 4d. As a matter of fact, the methane conversion rate continuously decreases during the first 4 h on stream, and afterwards the activity remains essentially constant. At quasi-steady state, after 15 h on stream, the methane conversion rate for Ir/CeO<sub>2</sub>-IWI is about 30% lower to that measured for Ir-CeO<sub>2</sub>-oxred. The initial deactivation of Ir/CeO<sub>2</sub>-IWI in SRM could be caused by both the slight agglomeration of Ir particles and/or their partial diffusion in the ceria carrier, as suggested by HRTEM micrographs (Fig. 1f). When H<sub>2</sub>S is added to the feed, Ir/CeO<sub>2</sub>-IWI shows a similar behavior as Ir-CeO<sub>2</sub>-oxred, the differences in activity being smaller than in the absence of H<sub>2</sub>S. Upon removal of H<sub>2</sub>S from the reaction feed, the catalytic activity of Ir/CeO<sub>2</sub>-IWI is progressively restored, reaching a slightly lower level than before H<sub>2</sub>S exposure.

These results confirm that ceria does not simply act as an inert carrier, but intervenes synergistically with Ir in the catalytic process. While the partial deactivation in response to the introduction of sulfur suggests the direct poisoning of the Ir active sites, the CeO<sub>2</sub> may provide sulfidation sites, keeping partly the sulfur away from the metal-support interface, where the reaction takes place. In this way, when CeO<sub>2</sub> is used as carrier for Ir, the latter becomes resistant to irreversible poisoning by sulfur. Thus, such a catalyst could be a good candidate for applications where accidental breakthroughs of sulfur compounds through the sulfur traps cannot be excluded.

Finally, having in mind the high activity of Rh in SRM based on literature reports [51] (Table 1), the performances of Ir-CeO<sub>2</sub>-oxred were compared with those of a Rh-CeO<sub>2</sub>-oxred catalyst. As shown by Fig. 4e, Rh-CeO<sub>2</sub> is less efficient in SRM under the conditions used here. The CH<sub>4</sub> conversion rate increases by a factor of 3 during the first 10 h of reaction, then remains constant (see also Table S1). The maximum activity is 4 and 3 times lower than those of Ir-CeO<sub>2</sub>-oxred and Ir/CeO<sub>2</sub>-IWI catalysts, respectively. As expected, when tested in the presence of H<sub>2</sub>S, the activity of Rh-CeO<sub>2</sub> sharply decreases. When the sulfur is removed from the gas phase, the activity of Rh-CeO<sub>2</sub> increases much more slowly than for Ir-ceria catalysts, and the catalyst never recovers its initial activity within reasonable time.

To summarize, the progress in restoring activity decreases as follows, as also shown by Table S3: Ir-CeO<sub>2</sub>-oxred > Ir/CeO<sub>2</sub>-IWI > Rh-CeO<sub>2</sub> > Ir/ASA. The differences observed in the recovery behavior of Ir- and Rh-ceria catalysts may arise from less stable Ir-S bond than the Rh-S one, under the strongly reducing experimental conditions employed.

### 3.4. Role of Ir and H<sub>2</sub>S, as revealed by CH<sub>4</sub>-TPR and XPS

The effect of the thermal treatment applied to Ir-CeO<sub>2</sub>, as well as the role of iridium and sulfur in the peculiar reactivity of CeO<sub>2</sub>, is further illustrated by the dynamic interaction between the catalytic surface and the reducing component of the reaction mixture (CH<sub>4</sub>), as investigated by CH<sub>4</sub>-TPR. The TPR profiles given in Fig. 5a and b were obtained for the fresh CeO<sub>2</sub> and Ir-CeO<sub>2</sub> samples, respectively, after an activation step in inert atmosphere at 900 °C (as before SRM tests). Fig. 5c and d shows CH<sub>4</sub>-TPR profiles for the CeO<sub>2</sub> and Ir-CeO<sub>2</sub>-oxred tested in SRM in the presence of 220 ppm H<sub>2</sub>S, respectively. In this case, before carrying the CH<sub>4</sub>-TPR measurements, the samples were purged at 750 °C in nitrogen for 5 min and quenched to room temperature in flowing N<sub>2</sub>.

Fig. 5a shows that CH<sub>4</sub> starts to react with ceria at 600 °C by producing traces amounts of CO<sub>2</sub>. H<sub>2</sub> and CO are formed from

630 °C, and their yields increase with temperature. The amount of CO formed during TPR ( $2.64 \text{ mmol g}^{-1} \text{ cat}$ ) markedly exceeds that of CO<sub>2</sub> ( $0.08 \text{ mmol g}^{-1} \text{ cat}$ ). The total oxygen content of CeO<sub>2</sub> being  $11.6 \text{ mmol g}^{-1}$ , the formation of CO<sub>x</sub> accounts for a ceria reduction degree of 23%. This confirms that CH<sub>4</sub> can reduce Ce<sup>4+</sup> sites into Ce<sup>3+</sup>, and that the bulk lattice oxygen of ceria is extensively involved in CO and CO<sub>2</sub> formations.

The addition of iridium to ceria is expected to catalyze both the dissociative adsorption of methane and the CeO<sub>2</sub> surface reduction, resulting in a downshift and broadening of the TPR peaks, as already noted for metal/ceria catalysts [52–54]. Indeed, in Fig. 5b, the TPR profiles for Ir-CeO<sub>2</sub>-inert and -oxred show a more complex shape than for pure CeO<sub>2</sub>, consisting of two main peaks (wider for Ir-CeO<sub>2</sub>-oxred), with a shoulder at low temperature (ca. 470 °C). These features, whose position, shape and intensity depend on the thermal treatment applied after synthesis, extend in the 350–900 °C temperature range. Overall, the products form at lower temperature (by 80 °C) in the case of Ir-CeO<sub>2</sub>-oxred, suggesting a higher reactivity of this catalyst toward methane, which is directly correlated with the SRM activity (Fig. 2).

Comparing Fig. 5a and b, the appearance of the low-temperature shoulder can be attributed to the reaction between CH<sub>4</sub> and surface oxygen species of ceria in contact with iridium sites. The low-temperature CO peak, only observed for Ir-CeO<sub>2</sub> catalysts, is assigned to the methane spilt over ceria after dissociative chemisorption on Ir [24]. Furthermore, as seen from the comparison of the high-temperature peak positions between Fig. 5a and b, the presence of Ir favors the interaction of CH<sub>4</sub> with bulk lattice oxygen species of ceria, which takes place at lower temperature than in the absence of Ir. The surface reduction of ceria, facilitated by the presence of Ir, creates oxygen vacancies and increases the ability of CeO<sub>2</sub> to release bulk oxygen by accelerating the diffusion of oxygen ions.

In Fig. 5c, it is seen that the onset of CO formation over ceria contacted with H<sub>2</sub>S takes places at 600 °C, versus 630 °C for the unexposed sample. The other remarkable difference is the split of the profile into two reduction/reaction peaks centered at ca. 770 °C and 890 °C. The appearance of the 770 °C peak suggests the existence of catalytic sites with enhanced reactivity toward methane on CeO<sub>2</sub> exposed to H<sub>2</sub>S. This new peak can be attributed to easier CH<sub>4</sub> activation and correlates with the increased SRM activity of ceria in the presence of sulfur (Fig. 4a). It is important to note here that a similar profile was obtained after 17 h of reaction in the presence of H<sub>2</sub>S. This means that the above-mentioned structural changes, accompanied by the formation of new sites with increased activity, take place in the first stage of the reaction, and are independent of the reaction time in the presence of H<sub>2</sub>S.

At variance from the behavior of CeO<sub>2</sub>, the exposure of Ir-CeO<sub>2</sub>-oxred to H<sub>2</sub>S results in the suppression of the low-temperature TPR peak, as can be seen from the comparison between Fig. 5b and d. As already discussed, the activity of Ir-CeO<sub>2</sub>-oxred was decreased by more than seven times after introduction of sulfur in the stream. This suggests that sulfur suppresses the low-temperature reaction pathway between methane and surface oxygen discussed above, in correlation with the loss of SRM activity (Fig. 4b). The remaining CH<sub>4</sub> consumption is characterized by intense H<sub>2</sub> and CO peaks centered at 730 °C, i.e. 40 °C lower than the new reduction peak observed for CeO<sub>2</sub> when contacted with H<sub>2</sub>S. This result is again in qualitative agreement with the activity difference between Ir-CeO<sub>2</sub> and CeO<sub>2</sub> tested in the presence of H<sub>2</sub>S.

Finally, XPS was used to get insight into the sulfur-containing adsorbed species on the spent CeO<sub>2</sub> and Ir-CeO<sub>2</sub>-oxred powders. Any exposure of the samples to ambient air was avoided during the transfer (see Section 2). The Ce 3d, Ir 4f, and S 2p core level signals for the spent samples are shown in Fig. 6. Fig. 6a reveals the presence of cerium in both IV and III oxidation states, in

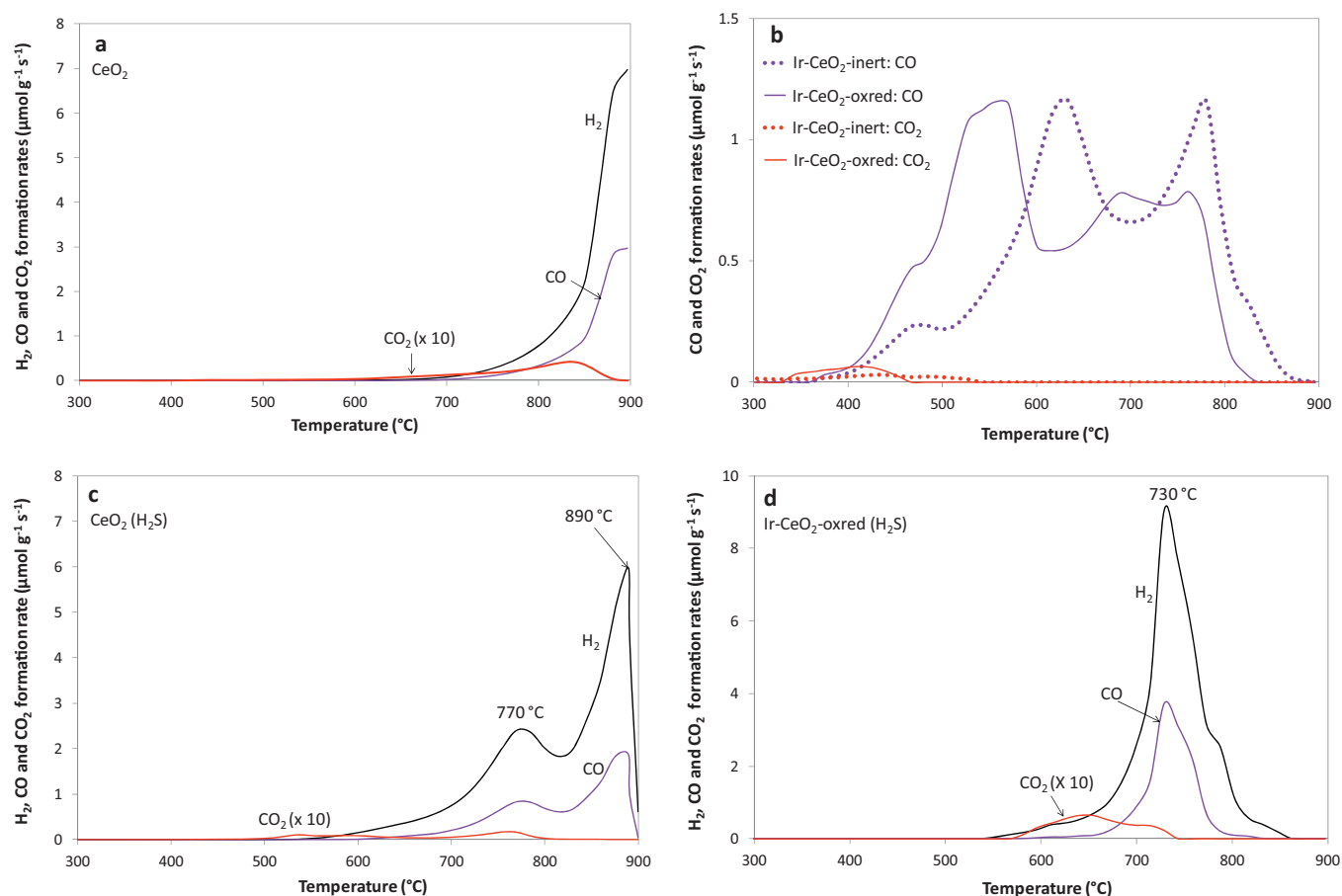


**Fig. 5.** H<sub>2</sub>, CO, and CO<sub>2</sub> formation rates during CH<sub>4</sub>-TPR experiments. (a) CeO<sub>2</sub>; (b) Ir-CeO<sub>2</sub>-inert and Ir-CeO<sub>2</sub>-oxred; (c) CeO<sub>2</sub> tested during 2 h in SRM in the presence of 220 ppm H<sub>2</sub>S (SRM conditions: same as in Fig. 2). (d) Ir-CeO<sub>2</sub>-oxred tested as in (c).

similar proportions in both powders: 8 and 7% Ce<sup>3+</sup> for CeO<sub>2</sub> and Ir-CeO<sub>2</sub>-oxred, respectively. These values were confirmed when O1s core-level spectra (not shown) were used as another source of information on Ce oxidation states. Due to the dopant level amount of Ir phase used in this work, no evidences on the type of Ir-O-Ce entities formed at the Ir-CeO<sub>2</sub> interface could be obtained. Fig. 6c reveals an Ir 4f<sub>7/2</sub> component centered around 61.2 eV. From literature reports [55], the Ir 4f<sub>7/2</sub> peaks for iridium sulfide and Ir<sup>0</sup> are centered at 63.2 and 60.7 eV, respectively. The peak at 61.2 eV can be assigned to Ir metal in interaction with the cerium oxide, and possibly partly covered by chemisorbed sulfur. This result explains

the higher activity of Ir-CeO<sub>2</sub>-oxred in CH<sub>4</sub>/H<sub>2</sub>O/H<sub>2</sub>S reaction when compared with pure ceria, in agreement with CH<sub>4</sub>-TPR findings. Although no evidence of the presence of Ir sulfide is provided by XPS data, the presence of such a phase cannot be ruled out due to the low amount of Ir in the catalyst.

The S 2p spectrum, centered at 167.8 eV for both CeO<sub>2</sub> and Ir-CeO<sub>2</sub>-oxred, is approximately 4 eV wide at half-maximum, indicating that it is composed of several oxidation states. Although peak deconvolution was not performed due to the low signal/noise ratio, the measured binding energy is characteristic of sulfite (S<sup>4+</sup>) and sulfate (S<sup>6+</sup>) species [56]. Interestingly, in a previous study [38],

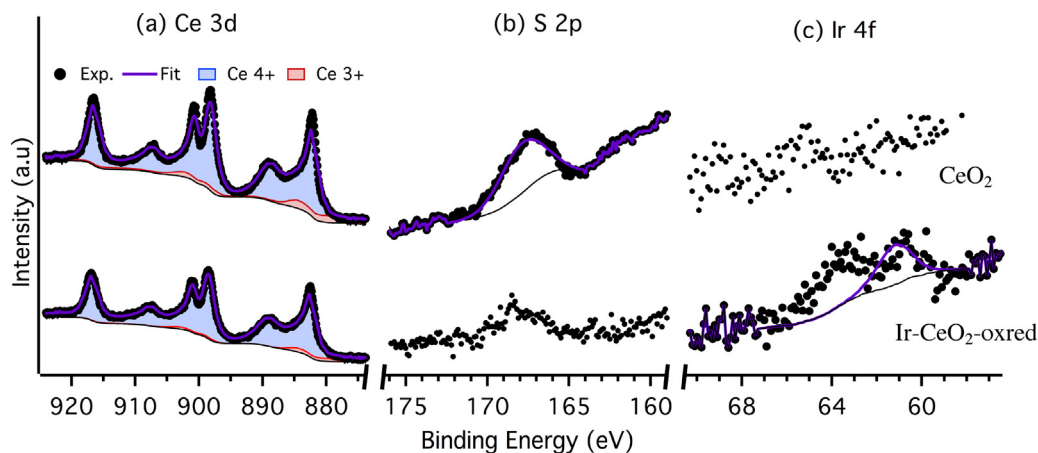


**Fig. 6.** XPS spectra after H<sub>2</sub>S exposure of CeO<sub>2</sub> (top) and Ir-CeO<sub>2</sub>-oxred (bottom) samples during CH<sub>4</sub>/H<sub>2</sub>O reaction at 750 °C.

the formation of  $S^{6+}/S^{4+}$  species was not observed after interaction of sulfur with a commercial  $Ce_{0.9}Gd_{0.1}O_{2-\delta}$  powder until maximum SRM activity was reached (this sample was tested in the same conditions as those reported here). In the present case, this means that sulfate/sulfite species, although detected on spent  $CeO_2$ , do not play any role in promoting the catalyst activity in the presence of  $H_2S$ . In other words, these compounds are only spectator species. The absence of an oxysulfide crystalline phase ( $Ce_2O_2S$ ) as revealed by XPS and XRD explains the highly stable activity of  $CeO_2$  when tested in  $CH_4/H_2O$  reaction in the presence of  $H_2S$ .

#### 4. Conclusions

This study demonstrates the relevance of using one-pot solution combustion synthesis for easy preparation of active Ir– $CeO_2$  catalysts for the steam reforming of methane. The thermal treatment applied to the catalyst plays a key role in creating active iridium surface sites. The optimal treatment of Ir– $CeO_2$  consists of oxidation at 300 °C followed by reduction at 500 °C. After such a procedure, Ir is present in the form of ca. 2 nm-sized particles, which are not affected by the severe conditions used in SRM. In that way, the optimized catalyst is more active and stable than its counterpart synthesized by conventional incipient wetness impregnation.

For SOFC applications integrating an electrocatalytic dissociation unit under GIR operation mode, catalysts with moderate activity in SRM, but highly resistant against the formation of carbon deposits and the irreversible poisoning by  $H_2S$ , are required. Carbon forms in little amount on the studied catalyst, making it stable on stream. Although the temporary collapse of the catalyst activity cannot be avoided when exposed to  $H_2S$ , Ir– $CeO_2$  exhibits a significant residual activity, which can enable stable cell operation during accidental breakthroughs of sulfur compounds through the sulfur traps. The catalyst almost fully recovers its initial activity upon replacement of the sulfur-containing stream with the original sulfur-free methane/water mixture.

#### Acknowledgements

LP and TSN acknowledge the French National Research Agency (ANR) for its financial support under the ANR-11-BS10-009 DINAMIC project. LP thanks F. Morfin for fruitful discussions on combustion methods. The authors thank F. Bosselet and Y. Aizac for XRD analysis, B. Jouguet for TG measurements, N. Cristin and P. Mascunan for chemical analyses, C. Lorentz for CHNS analysis, and L. Burel for SEM observations. E. Pouliquen is acknowledged for her participation to this project. GP thanks the CNRS for the financial support accompanying her Chaire d'Excellence position. Thanks are due to the CLYM for the access to the FEI Titan microscope (CLYM is supported by the CNRS, the "Grand Lyon" and the Rhône-Alpes Region).

#### Appendix A. Supplementary data

Supplementary data associated with this article can be found, in the online version, at <http://dx.doi.org/10.1016/j.apcatb.2014.11.024>.

#### References

- [1] X. Zhang, S.H. Chan, G. Li, H.K. Ho, J. Li, Z. Feng, J. Power Sources 195 (2010) 685–702.
- [2] Y. Chen, S. Chen, G. Hackett, H. Finklea, X. Song, K. Gerdes, Solid State Ionics 204–205 (2011) 87–90.
- [3] Y.R. Dar, P. Vijay, M.O. Tadé, R.J. Datta, Electroanal. Chem. 677–680 (2012) 15–23.
- [4] C.M. Grgicak, R.G. Green, J.B. Giorgi, J. Power Sources 179 (2008) 317–328.
- [5] C.J. Laycock, J.Z. Staniforth, R.M. Ormerod, Dalton Trans. 40 (2011) 5494–5504.
- [6] Z. Zhan, S.A. Barnett, Science 308 (2005) 844–847.
- [7] S. Georges, G. Parrou, M. Henault, J. Fouletier, Solid State Ionics 177 (2006) 2109–2112.
- [8] P. Vernoux, J. Guindet, M. Kleitz, J. Electrochem. Soc. 145 (1998) 3487–3492.
- [9] J.-M. Klein, M. Hénault, P. Gélén, Y. Bultel, S. Georges, Electrochem. Solid State Lett. 11 (2008) B144–B147.
- [10] S.D. Nobrega, P. Gelin, S. Georges, M.C. Steil, B.L. Augusto, F.B. Noronha, F.C. Fonseca, J. Electrochem. Soc. 161 (2014) F354–F359.
- [11] G. Jones, J.G. Jakobsen, S.S. Shim, J. Kleis, M.P. Andersson, J. Rossmeisl, F. Abild-Pedersen, T. Bligaard, S. Helveg, B. Hinnemann, J.R. Rostrup-Nielsen, I. Chorkendorff, J. Sehested, J.K. Nørskov, J. Catal. 259 (2008) 147–160.
- [12] J.R. Rostrup-Nielsen, J.H.B. Hansen, J. Catal. 144 (1993) 38–49.
- [13] J. Geest Jakobsen, Tommy L. Jørgensen, Ib Chorkendorff, Jens Sehested, Appl. Catal. A: Gen. 377 (2010) 158–166.
- [14] L.S.F. Feio, C.E. Hori, S. Damyanova, F.B. Noronha, W.H. Cassinelli, C.M.P. Marques, J.M.C. Bueno, Appl. Catal. A: Gen. 316 (2007) 107–116.
- [15] X. Wang, R.J. Gorte, Appl. Catal. A: Gen. 224 (2002) 209–218.
- [16] M.A. Soria, C. Mateos-Pedrero, I. Rodríguez-Ramos, A. Guerrero-Ruiz, Catal. Today 171 (2011) 126–131.
- [17] J. Wei, E. Iglesia, J. Phys. Chem. B 108 (2004) 7253–7262.
- [18] M. Zepiéri, P.L. Villa, N. Verdone, M. Scarsella, P. De Filippis, Appl. Catal. A: Gen. 387 (2010) 147–154.
- [19] M.H. Halabi, M.H.J.M. de Croon, J. van der Schaaf, P.D. Cobden, J.C. Schouten, Appl. Catal. A: Gen. 389 (2010) 68–79.
- [20] D.A.J.M. Ligthart, R.A. van Santen, E.J.M. Hensen, J. Catal. 280 (2011) 206–220.
- [21] J. Wei, E. Iglesia, J. Catal. 225 (2004) 116–127.
- [22] V.B. Mortola, S. Damyanova, D. Zanchet, J.M.C. Bueno, Appl. Catal. B: Environ. 107 (2011) 221–236.
- [23] J. Wei, E. Iglesia, J. Phys. Chem. B 108 (2004) 4094–4103.
- [24] J. Wei, E. Iglesia, Phys. Chem. Chem. Phys. 6 (2004) 3754–3759.
- [25] A. Berman, R.K. Karn, A. Epstein, Appl. Catal. A: Gen. 282 (2005) 73–83.
- [26] R. Craciun, B. Shereck, R.J. Gorte, Catal. Lett. 51 (1998) 149–153.
- [27] B. Höhle, S.V. Andrian, Th. Grube, R. Menzer, J. Power Sources 86 (2000) 243–249.
- [28] J. Toyir, P. Gélén, H. Belatel, A. Kaddouri, Catal. Today 157 (2010) 451–455.
- [29] G. Postole, K. Girona, J. Toyir, A. Kaddouri, P. Gélén, Fuel Cells 12 (2012) 275–287.
- [30] S.L. González-Cortés, F.E. Imbert, Appl. Catal. A: Gen. 452 (2013) 117–131.
- [31] U.-E.-S. Amjad, A. Vita, C. Galletti, L. Pino, S. Specchia, Ind. Eng. Chem. Res. 52 (2013) 15428–15436.
- [32] M.S. Hegde, G. Madras, K.C. Patil, Acc. Chem. Res. 42 (2009) 704–712.
- [33] B. Murugan, A.V. Ramaswamy, D. Srinivas, C.S. Gopinath, V. Ramaswamy, Chem. Mater. 17 (2005) 3983–3993.
- [34] T.-S. Nguyen, G. Postole, S. Lorient, F. Bosselet, L. Burel, M. Aouine, L. Massin, F. Morfin, P. Gélén, L. Piccolo, J. Mater. Chem. A 2 (2014) 19822–19832.
- [35] S.R. Jain, K.C. Adiga, V.R. Pai Verneker, Combust. Flame 40 (1981) 71–79.
- [36] C. Zhang, M.E. Grass, A.H. McDaniel, S.C. DeCaluwe, F. El Gabaly, Z. Liu, K.F. McCarty, R.L. Farrow, M.A. Linne, Z. Hussain, G.S. Jackson, H. Blumh, B.W. Eichhorn, Nat. Mater. 9 (2010) 944–949.
- [37] E. Ramirez-Cabrera, A. Atkinson, D. Chadwick, Appl. Catal. B: Environ. 47 (2004) 127–131.
- [38] G. Postole, F. Bosselet, G. Bergeret, N.S. Prakash, P. Gélén, J. Catal. 316 (2014) 149–163.
- [39] K. Bräjter, K. Szonawska, Talanta 30 (1983) 471–474.
- [40] A. Gayen, K.R. Priolkar, P.R. Sarode, V. Jayaram, M.S. Hegde, G.N. Subbanna, S. Emura, Chem. Mater. 16 (2004) 2317–2328.
- [41] V.M. Gonzalez-Delacruz, F. Ternero, R. Pereniguez, A. Caballero, J.P. Holgado, Appl. Catal. A: Gen. 384 (2010) 1–9.
- [42] P. Bera, K.R. Priolkar, P.R. Sarode, M.S. Hegde, S. Emura, R. Kumashiro, N.P. Lalla, Chem. Mater. 14 (2002) 3591–3601.
- [43] Y. Nagai, T. Hirabayashi, K. Dohmae, N. Takagi, T. Minami, H. Shinjoh, S. Matsumoto, J. Catal. 242 (2006) 103–109.
- [44] R.W. Verhoeft, D. Kelly, C.B. Mullins, W.H. Weinberg, Surf. Sci. 287 (1993) 94–98.
- [45] G. Henkelman, H. Jonsson, Phys. Rev. Lett. 86 (2001) 664–667.
- [46] Y. Huang, A. Wang, L. Li, X. Wang, D. Su, T. Zhang, J. Catal. 255 (2008) 144–152.
- [47] N. Laosiripojana, S. Charojrochkul, P. Kim-Lohsoontorn, S. Assabumrungrat, J. Catal. 276 (2010) 6–15.
- [48] M. Guenin, P.N. Da Silva, R. Frety, Appl. Catal. 27 (1986) 313–323.
- [49] Z. Vit, Appl. Catal. A: Gen. 322 (2007) 142–151.
- [50] S. Nassreddine, L. Massin, M. Aouine, C. Geantier, L. Piccolo, J. Catal. 278 (2011) 253–265.
- [51] R.J. Farrauto, Y. Liu, W. Ruettinger, O. Ilinich, L. Shore, T. Giroux, Catal. Rev. 49 (2007) 141–196.
- [52] H.C. Yao, Y.F.Y. Yao, J. Catal. 86 (1984) 254–265.
- [53] C. Xie, Y. Chen, Y. Li, X. Wang, C. Song, Appl. Catal. A: Gen. 390 (2010) 210–218.
- [54] L. Tournayan, N.R. Marcilio, R. Frety, Appl. Catal. 78 (1991) 31–43.
- [55] A. Infantes-Molina, A. Romero-Pérez, E. Finocchio, G. Busca, A. Jiménez-López, E. Rodríguez-Castellón, J. Catal. 305 (2013) 101–117.
- [56] E.J. Romano, K.H. Schulz, Appl. Surf. Sci. 246 (2005) 265–270 (and the references there in).